ADAPTIVE TRAINING OF INRS VIA PRUNING AND DENSIFICATION

Anonymous authors
Paper under double-blind review

ABSTRACT

Encoding input coordinates with sinusoidal functions into multilayer perceptrons (MLPs) has proven effective for implicit neural representations (INRs) of low-dimensional signals, enabling the modeling of high-frequency details. However, selecting appropriate input frequencies and architectures while managing parameter redundancy remains an open challenge, often addressed through heuristics and heavy hyperparameter optimization schemes. In this paper, we introduce AIRe (**A**daptive **I**mplicit neural **Re**presentation), an adaptive training scheme that refines the INR architecture over the course of optimization. Our method uses a neuron pruning mechanism to avoid redundancy and input frequency densification to improve representation capacity, leading to an improved trade-off between network size and reconstruction quality. For pruning, we first identify less-contributory neurons and apply a targeted weight decay to transfer their information to the remaining neurons, followed by structured pruning. Next, the densification stage adds input frequencies to spectrum regions where the signal underfits, expanding the representational basis. Through experiments on images and SDFs, we show that AIRe reduces model size while preserving, or even improving, reconstruction quality. Code and pretrained models will be released for public use.

1 INTRODUCTION

Implicit neural representations (INRs) have emerged as a powerful framework for modeling low-dimensional signals – such as images and signed distance functions (SDFs) – by encoding them directly in the parameters of neural networks (Sitzmann et al., 2020; Tancik et al., 2020; Saragadam et al., 2023; Dam et al., 2025). Instead of storing signals discretely, INRs represent them as continuous functions, mapping input coordinates $\mathbf{x}$ to a network predicting the corresponding signal value. To capture high-frequency content, these networks typically employ two key components: (1) projecting $\mathbf{x}$ into a list of sinusoidals $\sin(\omega\mathbf{x} + \varphi)$, where ω and φ denote the input frequencies and phase shifts, and (2) using periodic activation functions throughout the network layers. This combination enables INRs to represent fine details that standard ReLU-based MLPs struggle to learn due to their spectral bias (Tancik et al., 2020; Sitzmann et al., 2020).

Choosing an appropriate network architecture and input frequencies ω to accurately and compactly fit a target signal is a challenging task. Most prior work has addressed this by enhancing the expressiveness of INRs via tailored initialization schemes and specialized activation functions. For example, Zell et al. (2022) leveraged an initialization based on Fourier series to control the network's spectrum, enhancing its ability to represent fine-grained details. TUNER (Novello et al., 2025) provided a theoretical justification for this approach and introduced a training procedure to bandlimit the spectrum dynamically. FINER (Liu et al., 2024), on the other hand, employed a modified sine activation combined with bias initialization, allowing the modeling of high-frequency components. Despite these advances, selecting a compact yet expressive architecture a priori remains difficult: undersized networks tend to underfit the data, while oversized ones often lead to training instabilities and increased susceptibility to overfitting.

To address this challenge, we introduce **AIRe** (**A**daptive **I**mplicit neural **Re**presentation), a training framework that progressively adapts a potentially overparametrized INR to the target data through two complementary operations: *pruning* and *densification* of neurons. For pruning, we evaluate the contribution of each neuron using a customizable criterion (e.g. weight norms) to identify the

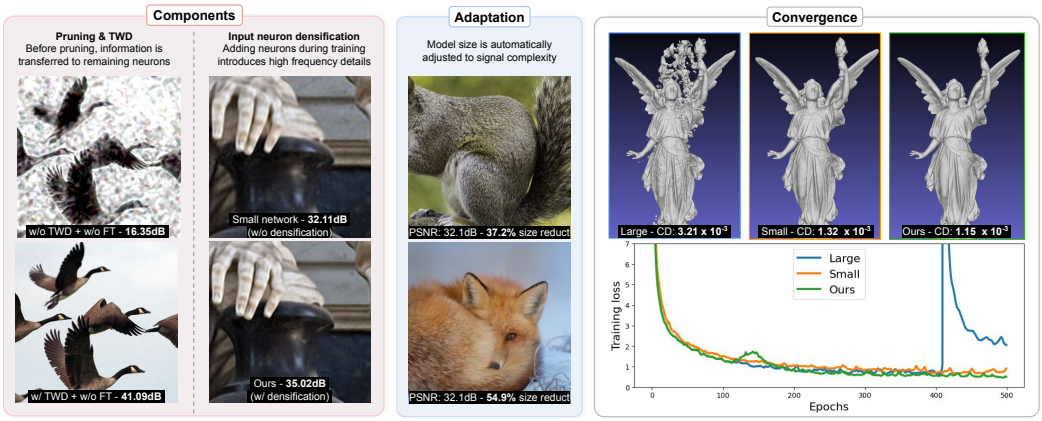

Figure 1: We present AIRe, a robust training method that adaptively fits the INR architecture to the target signal through two complementary mechanisms: (i) pruning with targeted weight decay (TWD) which mitigates parameter redundancy and fine tuning (FT) dependence by transferring information prior to structured neuron removal (see birds), and (ii) input frequency densification, which augments the representation basis, enhancing convergence and details fidelity (see hand). We compare three strategies: (i) an overparameterized SIREN model with standard training (*large network*), (ii) a model adapted with AIRe (**Ours**), and (iii) a *small network* fitted with standard training. AIRe improves reconstruction accuracy while producing more compact networks (blue box), and enhances training convergence in settings where overparameterization leads to divergence (see statue box).

most redundant ones. To transfer information from these low-contributing neurons to more relevant ones, we propose a novel *targeted weight decay* (TWD) mechanism, which penalizes their weights prior to structured removal. Once this transfer is induced, the targeted neurons are pruned. For densification, we introduce new input frequencies in underfit regions of the spectrum, expanding the network's representational capacity when necessary. By dynamically aligning model complexity with the input data, AIRe finds compact INRs that accurately reproduce the target signal. We showcase some of AIRe's results in Figure 1, illustrating strong performance in reconstruction quality, model compactness, and training stability. **Our main contributions are:**

- A general framework for the adaptive training of INRs, driven by pruning and densification. The pruning component brings principles from neural network pruning to the INR setting, while also introducing a novel targeted weight decay (TWD) strategy to preserve quality during neuron removal (see Figure 5). For densification, we add new input frequencies in underfit spectral regions, enhancing representational capacity (Table 4). Combined, these components enable accurate signal fitting with compact, data-adaptive architectures (Table 1).
- A theoretical analysis of both pruning and densification mechanisms for INRs. In particular, we leverage a harmonic expansion of sinusoidal neural networks (Theorem 1) to derive principled densification schemes, and prove stability of our neural networks under magnitude-based pruning (Theorem 2). Together, these promote densification and pruning mechanisms that mitigate divergence during training (cf. Figure 4).
- An empirical evaluation of AIRe across a range of image fitting and 3D shape reconstruction benchmarks. We show that AIRe consistently outperforms both the standard neural network training pipeline (see Table 1) as well as recent adaptive training methods (Table 2) in terms of the accuracy-efficiency trade-off.

2 Related Work

INRs emerged as a modern paradigm for learning low-dimensional signals such as images (Chen et al., 2021; Shi et al., 2024; Shah and Sitawarin, 2023; Kania et al., 2024; Han et al., 2025; Lee et al., 2021; Jayasundara et al., 2025), image morphing (Schardong et al., 2024; Bizzi et al., 2025), SDFs (Yang et al., 2021; Novello et al., 2022; Schirmer et al., 2024), displacement fields (Yifan et al.,

2021), surface animation (Mehta et al., 2022; Novello et al., 2023), and multiresolution signals (Paz et al., 2023; Saragadam et al., 2022; Lindell et al., 2022; Wu et al., 2023). On the methodological side, several works have explored the representation capacity of INRs (Mehta et al., 2021; Yüce et al., 2022; Saratchandran et al., 2025), as well as the critical role of initialization strategies (Novello, 2022; Paz et al., 2024; Saratchandran et al., 2024; Finn et al., 2017; Yeom et al., 2024).

Neural network pruning has long been of interest to the machine learning community (LeCun et al., 1989; Hassibi et al., 1993; Thimm and Fiesler, 1995; Frankle and Carbin, 2019; Hoefler et al., 2021; Blalock et al., 2020; Menghani, 2023). Classic approaches have relied on metrics such as weight magnitude, salience, or second-order derivatives, and are often followed by fine-tuning or regularization (e.g., weight decay) to preserve performance (Han et al., 2015; Tessier et al., 2022). However, it is known that methods often fail to generalize beyond their original settings (Blalock et al., 2020). To the best of our knowledge, Zell et al. (2022) is the only prior work exploring the pruning (or adaptation) of INRs. Their method removes input neurons to select an appropriate representational basis, but they did not explore hidden neurons pruning. In contrast, our method adapts the model size to target redundancy in the signal detail content while choosing a fitting input frequency encoding.

Recent work has investigated ways to adapt network architectures during training. The lottery ticket hypothesis (Frankle and Carbin, 2019) suggests that sparse subnetworks within overparameterized models can perform just as well when trained independently. Building on this idea, RigL (Evci et al., 2020) dynamically adjusts connectivity by pruning and growing connections during training. Also of note is Gaussian Splatting and related works (Kerbl et al., 2023; Zhang et al., 2024; Waczyńska et al., 2024), whose training procedures are adaptive and feature densification and pruning mechanisms. Nevertheless, while promising, such strategies have not been studied in the context of INRs, where the objectives, data modalities, and inductive biases differ significantly from those in previous endeavors. In Table 2, we adapt these methods to the INR setting and compare them with AIRe, showing that our approach achieves superior results.

3 Adaptive Training of INRs

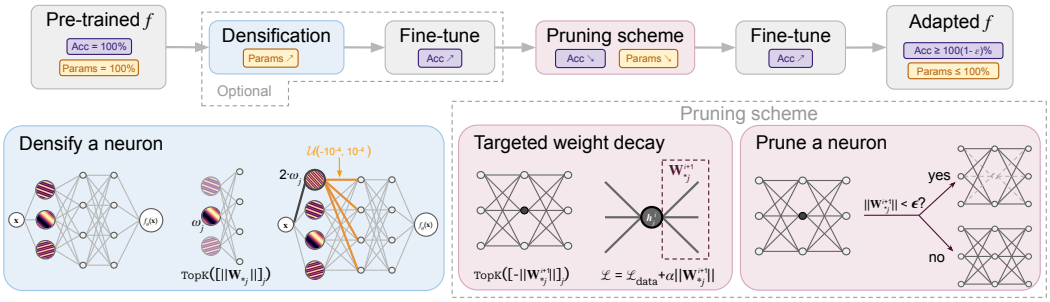

Figure 2: We present AIRe, a training framework that adapts network architecture through two theoretically grounded strategies: *densification* and *pruning*. For signals with rich frequency content, densification selects the most relevant input frequencies ω_j and expands the spectrum by augmenting ω with $2 \cdot \omega_j$. To reduce network size, pruning identifies candidate neurons via magnitude criterion, transfers information during training with a novel targeted weight decay (TWD) regularization, and removes neurons whose norm falls below a threshold ϵ. The function $\mathrm{TopK}(v)$ selects the K largest entries of v.

Our goal is to develop a training framework that dynamically adapts a sinusoidal INR architecture to the given data samples $\{\mathbf{x}_j, f_j\}$ from a low-dimensional signal f. Specifically, we want to adjust the size of a sinusoidal MLP of depth $d \in \mathbb{N}$ defined as $f(\mathbf{x}) = \mathbf{L} \circ \mathbf{S}^d \circ \cdots \circ \mathbf{S}^0(\mathbf{x})$, a composition of d sinusoidal layers $\mathbf{S}^i(\mathbf{x}) = \sin(\mathbf{W}^i\mathbf{x} + \mathbf{b}^i)$ parameterized by a weight matrix $\mathbf{W}^i \in \mathbb{R}^{n_{i+1} \times n_i}$ and a bias vector $\mathbf{b}^i \in \mathbb{R}^{n_{i+1}}$, followed by an affine layer $\mathbf{L}$. Observe that the first layer $\mathbf{S}^0$ maps the input coordinates $\mathbf{x}$ into a harmonic embedding of the form $\sin(\omega\mathbf{x} + \varphi)$, where we denote $\omega := \mathbf{W}^0$ as the matrix of *input frequencies* and $\varphi := \mathbf{b}^0$ as the vector of *phase shifts*.

Although the choice of $\{n_i\}_i$ is critical for determining network capacity, it is typically based on empirical heuristics. Moreover, a model with poorly initialized input frequencies ω may fail to

capture the full spectrum of the signal, leading to unsatisfactory reconstruction. To address these problems, we adapt a model architecture by adding and removing neurons. More precisely, we define the *ij-neuron* $h_j^i(\mathbf{x})$ of f as the j-th coordinate of the output of the i-th layer, that is,

$$h_j^{i+1}(\mathbf{x}) = \sin\big(\mathbf{W}_{j*}^{i+1}\sin(\mathbf{y}^i) + b_j^{i+1}\big), \tag{1}$$

where $\mathbf{y}^i$ denotes the linear transformation of the ith layer prior to activation. Then, we densify the input neurons by appending new ones to $\mathbf{h}^0(\mathbf{x})$, introducing novel frequencies to expand the spectral coverage. Finally, we employ a magnitude-based neuron pruning scheme to account for potential redundancy in parameters. Figure 2 provides an overview of AIRe.

3.1 Densification

Sinusoidal INRs employ an embedding layer parametrized by input frequencies ω which are passed through the network, generating additional frequencies, enriching the network's spectrum so as to mitigate spectral bias. However, the representation capacity of such networks is heavily dependent on the initialization of ω, which may lead to noisy reconstructions or slower training when done poorly. To mitigate this, we introduce a densification strategy for the set of input frequencies ω that identifies important generated frequencies (those with high amplitude in a certain trigonometric expansion of the network) and introduce them directly in the input frequencies ω, enriching the network.

To design this densification strategy, we must analyze the network spectrum. This can be done by a theorem of Novello et al. (2025), which provides a trigonometric expansion that facilitates this analysis.

Theorem 1. *The neuron h_j^{i+1} admits the following amplitude-phase expansion:*

$$h_j^{i+1}(\mathbf{x}) = \sum_{\mathbf{k}\in\mathbb{Z}^{n_i}} \alpha_{\mathbf{k}}(\mathbf{W}_{j*}^i)\,\sin\big(\langle\mathbf{k},\mathbf{y}^i\rangle + b_j^{i+1}\big), \quad \text{where} \quad |\alpha_{\mathbf{k}}(\mathbf{W}_{j*}^i)| \le \prod_l \frac{1}{|k_l|!}\left(\frac{|W_{jl}^{i+1}|}{2}\right)^{|k_l|} \tag{2}$$

Here, $\alpha_{\mathbf{k}}(\mathbf{W}_{j*}^i) = \prod_l J_{k_l}(W_{jl}^{i+1})$ is the product of Bessel functions.

This result shows that the composition of sinusoidal layers generates new frequencies of the form $\langle\mathbf{k},\omega\rangle$, depending solely on the input frequencies ω, with phase shifts determined by the biases $\{\varphi, \mathbf{b}^i\}$. Additionally, the amplitudes $\alpha_{\mathbf{k}}$ depend exclusively on the hidden weight matrices $\mathbf{W}^i$. Thus, the generated frequencies are governed by the input embedding, while the hidden parameters control the amplitudes and phase shifts. Moreover, from Equation 2 we observe that

$$\mathbf{h}^0(\mathbf{x}) = \left[\sum_{\mathbf{k}\in\mathbb{Z}^{n_0}} \alpha_{\mathbf{k}}\sin\left(\langle\mathbf{k},\omega\rangle\mathbf{x} + b_j\right)\right]_j \quad \text{with bias } b_j = \langle\mathbf{k},\varphi\rangle + b_j^1. \tag{3}$$

Thus, adding an input neuron with frequency ω' expands the layer spectrum from $\{\langle\mathbf{k},\omega\rangle\}_{\mathbf{k}}$ to $\{\langle\mathbf{k},\omega\rangle + l\cdot\omega'\}_{\mathbf{k},l}$. Since the input frequencies determine the network's generated frequencies, the densification of the input neurons can greatly increase the expressiveness of the overall network.

Equation 3 suggests a natural set of new input frequencies ω' to be added: multiples of input frequencies whose corresponding columns in the first hidden layer have high norm. Specifically, if the jth column W_{*j}^1 of the first hidden layer matrix $\mathbf{W}^1$ has a high norm, then the lowest multiples of its associated frequency ω_j tend to appear with larger amplitudes.[1] Therefore, during densification, we identify input frequencies ω_j whose corresponding columns W_{*j}^1 exhibit high norms, and we expand the set of input frequencies ω by adding their doubled counterparts $2\omega_j$, boosting the input frequencies and thus enriching the network's representation. As shown in Figure 10, after densification most of the newly added neurons become highly contributive to the reconstruction.

Finally, the corresponding new column in the hidden matrix $\mathbf{W}^1$ is initialized with random values drawn from a uniform distribution in the range $[-10^{-4}, 10^{-4}]$, ensuring a stable start for training. Finally, the network is retrained to fine-tune all parameters, allowing it to adapt to the extended frequency spectrum and fully leverage the increased representational capacity.

[1] This follows from Equation 3 and the fact that $|J_2(W_{ij}^1)| > |J_{k_j}(W_{ij}^1)|$ for most i, since Bessel functions are sorted by their order (Novello, 2022, Sec 2.2).

3.2 PRUNING

Determining an appropriately sized model capable of representing the target signal with quality is a key challenge when training sinusoidal INRs. Typically, large architectures are employed to ensure reconstruction accuracy, sacrificing model compactness. To address this, we design a pruning procedure that detects and removes redundant neurons during training.

First, we employ a magnitude-based criterion to identify uninformative neurons, a common strategy in classical network pruning. We now provide a formal justification of its validity for INRs: in sinusoidal MLPs, pruning neurons induces only a bounded perturbation to the overall function. This perturbation depends on the ∞-operator norms of the parameter changes and the norms of the subsequent layers.

Theorem 2. *Let f be a sinusoidal INR of depth d, and let $\widetilde{f}$ be the network obtained by perturbing the k-th hidden layer weights and biases to $\widetilde{\mathbf{W}}^k$ and $\widetilde{\mathbf{b}}^k$. Then,*

$$\sup_x \left\| f(x) - \widetilde{f}(x) \right\|_\infty \leq \left(\left\| \mathbf{W}^k - \widetilde{\mathbf{W}}^k \right\|_\infty + \left\| \mathbf{b}^k - \widetilde{\mathbf{b}}^k \right\|_\infty \right) \|\mathbf{L}\|_\infty \prod_{i=k+1}^{d} \|\mathbf{W}^i\|_\infty.$$

Theorem 2 formally guarantees that small modifications to a layer's parameters—such as pruning neurons with small outgoing weights—induce only proportionally small changes to the network's output. This justifies magnitude-based pruning both intuitively and theoretically. However, training directly with the reconstruction loss $\mathcal{L}_{\text{data}}$ (e.g. MSE) often leads to relatively few truly redundant neurons, even in overparametrized architectures. For better pruning, we employ a targeted weight decay (TWD) strategy that reduces the contribution from near-redundant neurons, turning them truly redundant. It consists of training the network f with the loss function,

$$\mathcal{L}_{\alpha,\mathcal{I}} = \mathcal{L}_{\text{data}} + \alpha \sum_{j \in \mathcal{I}} \|\mathbf{W}_{*j}^{i+1}\|_1, \quad \text{with} \quad \alpha \in [0, 1), \tag{4}$$

where $\mathcal{I} = \text{TopK}\left(\left[-\|\mathbf{W}_{*j}^{i+1}\|_1 \right]_j \right)$ are the K indices of the neurons with the smallest column norm.

Our procedure uses TWD to isolate low-impact neurons, ensuring that pruning remains consistent with the theoretical stability. Then, we select the neurons to remove by thresholding small ℓ_1 norms, e.g., pruning h_j^i if $\|\mathbf{W}_{*j}^{i+1}\|_1 = \|\mathbf{W}^{i+1} - \widetilde{\mathbf{W}}^{i+1}\|_\infty \leq \epsilon$ (where $\widetilde{\mathbf{W}}^{i+1}$ denotes the altered weight matrix), and fine-tune the network to recover performance. As illustrated in Figure 2, pruning a neuron $h_j^i(\mathbf{x})$ involves removing its outgoing connections. In practice, we mask only the entries of the j-th column $\mathbf{W}_{*j}^{i+1}$, which implicitly leaves unused the row $\mathbf{W}_{j*}^i$ and bias b_j^i. Note that pruning the input neurons may have greater impact on the reconstruction since we are deleting an input frequency; that is, we are eliminating many generated frequencies from the network spectrum.

4 EXPERIMENTS

We evaluate AIRe on adaptive training across three tasks: image fitting, surface reconstruction (SDFs), and novel view synthesis with NeRFs. Experiments are conducted on the DIV2K (Agustsson and Timofte, 2017), Stanford Repository (Curless and Levoy, 1996), and NeRF Synthetic (Mildenhall et al., 2021) datasets. We also study AIRe in a setup where the final architecture is fixed, demonstrating that our training procedure can improve reconstruction quality even when the reduced small architecture is known in advance. Finally, we perform ablation studies to validate the design choices underlying our method.

All models are implemented in PyTorch (Paszke et al., 2019) and optimized with Adam (Kingma and Ba, 2015).For simplicity, we denote a MLP by $[n_1, ..., n_{d+1}]$, where d is the number of hidden layers and n_i is the number of neurons in the i-th layer. The pruning threshold is set to $\epsilon = 0.01$, which prevents neurons with contributions above this value from being pruned; this threshold is fixed and applied uniformly across all layers.

Comparison with standard training. We compare AIRe against a baseline defined by the original, large initial architecture (overparametrized) trained with the standard neural network training pipeline,

showing that AIRe can reduce model size while maintaining reconstruction quality by finding more appropriate input frequencies. We evaluate this on images, SDFs, and NeRFs, adopting commonly used architectures for each task (SIREN and FINER). Table 1 shows that AIRe achieves substantial reductions in SIREN's model size while maintaining reconstruction quality, and in several cases even improving it.

Table 1: **Our method fits a compact INR to the target signal while preserving accuracy.** We evaluate AIRe ('Ours') against an overparametrized INR trained with the standard training pipeline ('Large') on images (with model size [512, 256, 256]), SDFs (with architecture $[256, 256, 256]$), and NeRF tasks (with size $[256, 128, 128]$), reporting PSNR and Chamfer Distance ($\times 10^2$). AIRe enables a strong reduction in model size, while preserving or even improving quality.

Imgs (DIV2K)	**Large PSNR↑**	**Ours PSNR↑**	**Size reduct.↑**	**SDFs** (Stanford)	**Large CD↓**	**Ours CD↓**	**Size reduct.↑**	**NeRF** (Synthetic)	**Large PSNR↑**	**Ours PSNR↑**	**Size reduct.↑**
#00	31.96	31.56	35.89%	Armadillo	0.62	0.63	73.30%	Lego	25.72	25.30	35.00%
#01	37.93	35.63	65.28%	Bunny	0.76	0.71	72.33%	Materials	23.71	23.62	30.86%
#02	30.76	29.17	52.39%	Dragon	0.73	0.61	70.33%	Ficus	24.23	24.82	26.83%
#03	37.40	35.04	56.80%	Buddha	0.59	0.56	41.27%	Hotdog	29.69	28.68	33.14%
#04	33.88	31.09	60.08%	Lucy	0.92	0.58	52.50%	Drums	22.17	22.02	39.09%

Comparison against existing pruning baselines. Table 2 reports a comparison with existing pruning approaches on the image representation task, using the same SIREN configuration as in Table 1. We evaluate two model-agnostic pruning methods, DepGraph (Fang et al., 2023) and RigL (Evci et al., 2020), as well as a baseline obtained by training a small architecture from scratch. We also compare against Zell et al. (2022), a method that initializes the first SIREN layer with a wide range of frequencies given by the Cartesian product between $[0, 1, \dots, L]$ and $[-L, \dots, L]$ for a chosen maximum frequency L. In our experiment, we set $L = 19$, yielding 780 input frequencies—substantially larger than the first-layer width of 512 used in AIRe. We train their model for 5,000 epochs and prune the input frequencies following the strategy described in their paper. The pruning rate of each method is set to approximately 25% of the original parameters, and we follow the hyperparameter choices reported in the respective papers. AIRe consistently outperforms these pruning methods, demonstrating its effectiveness for INR architecture adaptation over training.

Table 2: **Comparison of pruning criteria.** Results are on the image representation task.

Method	**PSNR↑**	**SSIM↑**
Small	34.60 ± 3.82	0.92 ± 0.03
DepGraph	27.56 ± 2.12	0.82 ± 0.04
RigL	34.29 ± 3.37	**0.95 ± 0.01**
Zell et al. (2022)	18.96 ± 1.92	0.39 ± 0.08
AIRe (ours)	**37.07 ± 3.74**	**0.95 ± 0.01**

4.1 AIRe vs. small networks

AIRe starts with a **large** architecture and progressively reduces its size during training, resulting in a **small** network. To evaluate how effectively AIRe leverages its architectures, we compare it against standard training applied directly to both the initial (large) architecture and the final (small) one. We conduct this evaluation for image fitting (DIV2K) and SDF reconstruction (Stanford Repository).

For the SDF reconstruction task, we follow the implementation in (Novello et al., 2022), training each network for 10^3 epochs, sampling 10^4 on-surface points and 10^4 off-surface points uniformly. Meshes are extracted from the trained SDFs via marching cubes with a resolution of 512^3, and all surfaces were normalized to $[-1, 1]^3$. For evaluation, we report the number of network parameters (Params) and the Chamfer Distance (CD) between reconstructed and ground-truth surfaces. We also evaluate AIRe without densification, as SDFs typically contain less details than other applications.

For training, we start with a large network $[256, 256, 256]$, trained from scratch for 200 epochs. We then select 192 neurons from the input layer and the first hidden layer and continue training with targeted weight decay (TWD) for 500 epochs. Finally, the selected neurons are pruned, and the resulting smaller network $[64, 64, 256]$ is retrained for 300 epochs. Table 3(left) shows that AIRe provides a better SDF reconstruction than the large network in all cases. We also highlight that our

Table 3: **AIRe vs. directly trained large and small networks.** We compare AIRe with standard training applied to large and small architectures on both SDF reconstruction (Stanford) and image fitting (DIV2K). Metrics are CD ($\times 10^2$) for SDFs and PSNR for images, along with parameter reduction relative to the large model. AIRe achieves accuracy comparable to or better than the large network while using the same reduced parameter budget as the small one.

Model (SDFs)	**Variant**	**CD (×10²) ↓**	**Size reduct. ↑**	**Model** (Images)	**Variant**	**PSNR ↑**	**Size reduct. ↑**
	Large	0.65 ± 0.11	-		Large	**39.59 ± 3.30**	-
SIREN	Small	0.89 ± 0.09	83.96%	SIREN	Small	34.60 ± 3.82	24.95%
	Ours	**0.64 ± 0.03**	83.96%		Ours	37.07 ± 3.74	24.95%
	Large	2.14 ± 0.41	-		Large	38.77 ± 2.98	-
FINER	Small	5.08 ± 3.51	83.96%	FINER	Small	38.87 ± 3.44	24.95%
	Ours	**0.88 ± 0.15**	83.96%		Ours	**39.91± 3.89**	24.95%

approach obtains similar or better accuracy compared to the initial, large network trained from scratch while using roughly between a third and a sixth of the network parameters for surface representation. Aditionally, we found that AIRe has a comparable time overhead ($76.8s$) compared to the large SIREN model ($76.0s$). Moreover, even when training a small architecture during $83.2s$, it performs worse than AIRe with 0.86×10^2 for CD metric. Figure 3 shows some qualitative comparisons of AIRe and the small architecture with standard training on the Armadillo, Buddha, and Lucy models, showing that AIRe provides, in general, a lower (bluer) distance from the ground-truth surface.

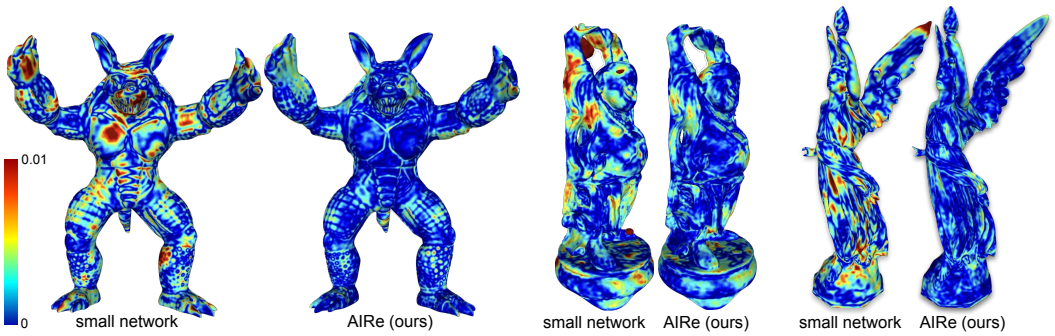

Figure 3: **Qualitative comparison of SDF reconstructions** on the Armadillo, Buddha, and Lucy models using a SIREN with $\omega_0 = 60$ and small network size $[64, 64, 256]$. Left: results of training the final small network directly. Right: results of AIRe. Colors indicate the distance from the ground-truth surface, from dark blue (0) to dark red (≥ 0.01). AIRe produces reconstructions that are consistently closer to the ground truth than those obtained by training the small network from scratch.

Additionally, AIRe mitigates divergence during the training of SDF models, as illustrated in Figure 4. We illustrate this by initializing a large network of size $[256, 256, 256, 256]$ and training it on the Armadillo for half the epochs with $\omega_0 = 60$ and small network architecture $[64, 64, 64, 256]$. Under standard training, the large network diverges, producing reconstructions with severe noise and artifacts. In contrast, AIRe yields a more accurate reconstruction despite using less than half the parameters of the initial model.

For the evaluation on the image fitting task, we use the FINER subset of the DIV2K dataset, randomly selecting 90% of the pixels of each image for training and using the remaining 10% for testing. Training is performed with Mean Square Error (MSE) loss, a batch size of $65{,}536$ pixels, and evaluation is based on Peak Signal-to-Noise Ratio (PSNR). All experiments use sinusoidal MLPs with $\omega_0 = 30$ trained for 5000 epochs. For AIRe, we first train for 250 epochs with MSE to capture low-frequency information, then add 128 new input neurons and fine-tune for 2000 epochs. Next, we train for 2250 epochs with TWD, prune 384 input neurons, and fine-tune the resulting network for an additional 500 epochs. The resulting small network of size $[256, 512, 512]$ is compared against a model of the same size trained from scratch with MSE for 5000 epochs.

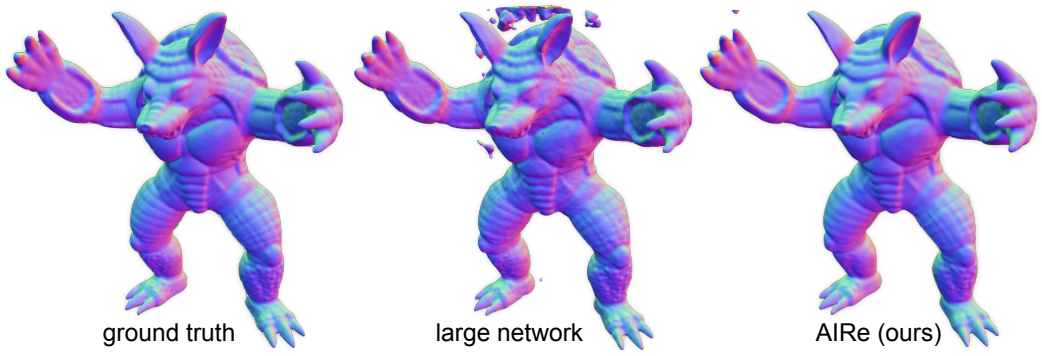

Figure 4: Qualitative comparison on the Armadillo. Left: ground truth. Middle: standard training of the large network, which diverges and produces noisy artifacts. Right: AIRe, which avoids divergence and yields a cleaner reconstruction with fewer parameters.

Table 3 (right) shows that AIRe applied to SIREN and FINER networks achieves better convergence than standard training applied directly to either large or small networks. AIRe improves mean accuracy by 2.47 dB on SIREN and 1.04 dB on FINER, consistently outperforming standard MSE training. These results demonstrate that AIRe effectively transfers information from the overparameterized model to its small counterpart.

4.2 Ablations

Effect of varying pruning rate. We now ablate key design choices of AIRe, focusing on the rate of pruning and densification during training. First, we analyze the effect of pruning on reconstruction quality. We compare the accuracy drop of an adapted INR relative to a pre-trained network of size $[512, 512, 512]$ (528K parameters), which achieves a PSNR of 43.67 dB. We apply AIRe to the same architecture, starting with standard training for 2250 epochs, followed by selecting $p\%$ of the input neurons and the first hidden neurons to prune ($p \in \{0.2, 0.4, 0.6, 0.8\}$) and training with TWD for another 2250 epochs. Finally, we prune the selected neurons and fine-tune the resulting network for 500 epochs, totaling 5000 epochs of adaptation.

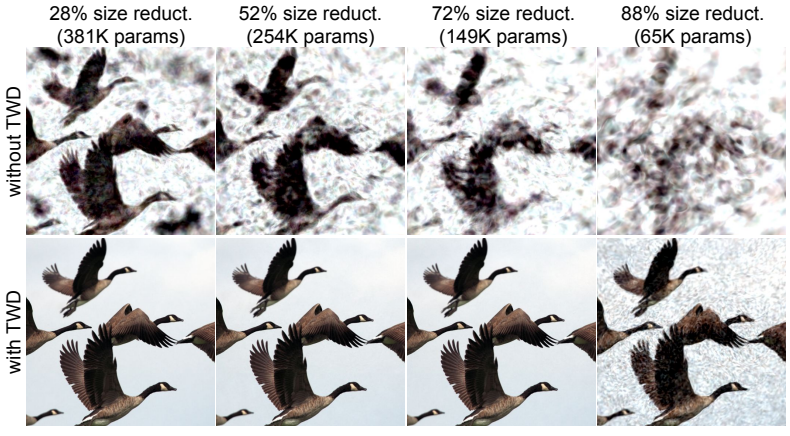

	Size reduct.	w/o TWD	w/ TWD
w/o FT	28%	14.35	43.43
	48%	15.61	40.28
	72%	14.07	41.25
	88%	14.00	21.60
w/ FT	28%	41.24	43.57
	48%	42.93	43.54
	72%	41.98	42.75
	88%	37.28	38.25

Figure 5: **TWD reduces the dependence of finetune (FT) when pruning.** TWD effectively transfers information before pruning. Left: qualitative results with 28%, 52%, 72%, and 88% of parameters pruned. The first row shows results without TWD, and the second row with TWD. Right: Table with the PSNR values for each case.

As shown in Figure 5, TWD enables effective transfer of information to the remaining neurons so that a pruned network (without fine-tuning) with only 28% of its weights still retains 92% of the original network's accuracy. In contrast, pruning without TWD leads to a severe degradation in image quality.

After full training, AIRe achieves a quality drop of less than 2.1% with just 28% of the parameters, compared to a 3.8% drop when TWD is removed from the pipeline.

With vs. without densification. We ablate the role of densification in our pipeline using the same configuration as Table 2, training all models for 5000 epochs on a subset of DIV2K. In Table 4, we compare: (i) a small architecture trained from scratch; (ii) a large model pruned (without densification) to match the small architecture; and (iii) our proposed AIRe scheme, which iteratively adds and removes input neurons until matching the small architecture. Pruning alone yields a modest accuracy gain for SIREN, while the *Densify+Prune* (AIRe) strategy provides a substantial boost. For FINER, pruning slightly improves reconstruction quality, but densification brings little benefit – consistent with the fact that FINER models are already more expressive and less dependent on additional frequency capacity.

Table 4: **Effect of pruning and densification** on SIREN and FINER networks (DIV2K).

Method	SIREN PSNR ↑	FINER PSNR ↑
Small	36.44 ± 4.20	40.84 ± 3.85
Prune	37.58 ± 3.77	41.80 ± 3.80
Densify+Prune	**39.47 ± 4.31**	**41.88 ± 4.24**

Pruning after densification vs. before densification. Intuitively, increasing model capacity before removing redundancies should improve convergence. To verify this, we train a network of size $[256, 512, 256]$ and compare two schedules: pruning before densification and pruning after densification. For *densify before prune*, we train for 400 epochs with MSE, add 128 input neurons, fine-tune for 200 epochs, train with TWD for 200 epochs, prune 50% of the first hidden neurons, and fine-tune for 1200 epochs. For *pruning before densify*, we train for 200 epochs with MSE, continue for 200 epochs with TWD, prune 50% of the first hidden neurons, fine-tune for 200 epochs, add 128 neurons, and finally fine-tune for 1400 epochs.

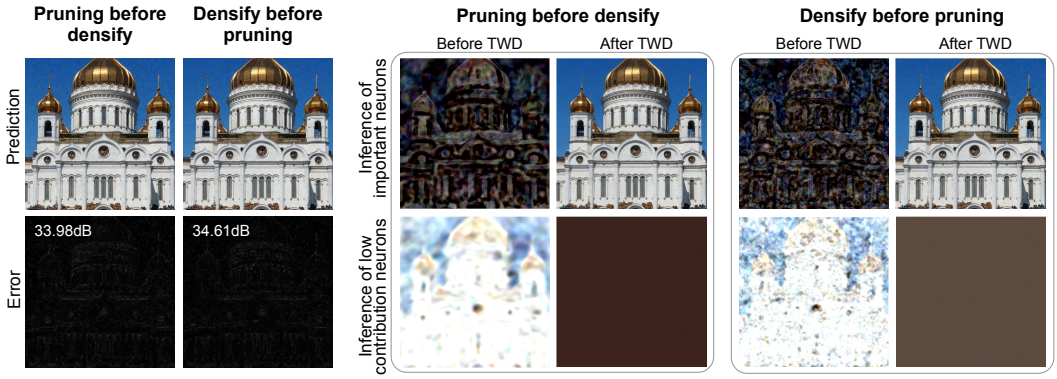

Figure 6: **Effect of pruning-before-densify and densify-before-pruning strategies.** Left: reconstructed signal and error map for each strategy. Right: information transfer during TWD. We visualize the model's inference when restricted to high-contribution neurons (top) and to low-contribution neurons (bottom), evaluated both before and after TWD. TWD offers strong information transfer in both configurations; however, in the densify-before-pruning case, the important neurons capture higher-frequency components, resulting in improved reconstruction quality.

The *pruning-before-densify* strategy achieves an average PSNR of 33.41 dB, whereas *densify-before-pruning* reaches 33.99 dB, confirming our intuition about the ordering of our components. Figure 6 (left) shows a prediction alongside its corresponding error map. On the right, we compare two inferences: the top row uses only parameters of neurons identified as important, while the bottom row uses only the weights of neuron deemed low-contribution. The important-neuron inference preserves most image details, preserving most of the spectral content. In contrast, the inference restricted to low-contribution neurons lacks detail and collapses toward a constant function durint TWD. Note how important neurons in the *densify-before-pruning* scheme contain more high frequency details than its counterpart in the *pruning-before-densify* strategy before the TWD.

5 Conclusion

We introduced AIRe, a dynamic training framework for implicit neural representations (INRs) that adaptively aligns network architecture with the complexity of the target signal. The framework integrates two complementary components: *pruning*, which removes redundant neurons to mitigate overparameterization, and *densification*, which expands the network's expressivity by selectively introducing new input frequencies based on a principled spectral analysis.

Our approach contributes toward automating architecture adaptation in INR learning, offering a more efficient and flexible alternative to static design choices. As future work, we aim to develop more advanced mechanisms for information transfer during pruning, extend our method to a broader class of architectures, and explore its applicability to more data modalities beyond images and surfaces.

References

Milton Abramowitz and Irene A Stegun. *Handbook of mathematical functions with formulas, graphs, and mathematical tables*, volume 55. US Government printing office, 1964.

Eirikur Agustsson and Radu Timofte. Ntire 2017 challenge on single image super-resolution: Dataset and study. In *2017 IEEE Conference on Computer Vision and Pattern Recognition Workshops (CVPRW)*, pages 1122–1131, 2017. doi: 10.1109/CVPRW.2017.150.

Arthur Bizzi, Matias Grynberg, Vitor Matias, Daniel Perazzo, João Paulo Lima, Luiz Velho, Nuno Gonçalves, João Pereira, Guilherme Schardong, and Tiago Novello. Flowing: Implicit neural flows for structure-preserving morphing. *arXiv preprint arXiv:2510.09537*, 2025.

Davis Blalock, Jose Javier Gonzalez Ortiz, Jonathan Frankle, and John Guttag. What is the state of neural network pruning? *Proceedings of machine learning and systems*, 2:129–146, 2020.

Yinbo Chen, Sifei Liu, and Xiaolong Wang. Learning continuous image representation with local implicit image function. In *Proceedings of the IEEE/CVF conference on computer vision and pattern recognition*, pages 8628–8638, 2021.

Brian Curless and Marc Levoy. A volumetric method for building complex models from range images. In *Proceedings of the 23rd annual conference on Computer graphics and interactive techniques*, pages 303–312, 1996.

Sumit Kumar Dam, Mrityunjoy Gain, Eui-Nam Huh, and Choong Seon Hong. High-frequency first: A two-stage approach for improving image inr. *arXiv preprint arXiv:2508.15582*, 2025.

Utku Evci, Trevor Gale, Jacob Menick, Pablo Samuel Castro, and Erich Elsen. Rigging the lottery: Making all tickets winners. In *International Conference on Machine Learning*, pages 2943–2952. PMLR, 2020.

Gongfan Fang, Xinyin Ma, Mingli Song, Michael Bi Mi, and Xinchao Wang. Depgraph: Towards any structural pruning. In *Proceedings of the IEEE/CVF conference on computer vision and pattern recognition*, pages 16091–16101, 2023.

Chelsea Finn, Pieter Abbeel, and Sergey Levine. Model-agnostic meta-learning for fast adaptation of deep networks. In *International conference on machine learning*, pages 1126–1135. PMLR, 2017.

Jonathan Frankle and Michael Carbin. The lottery ticket hypothesis: Finding sparse, trainable neural networks. In *International Conference on Learning Representations*, 2019. URL `https://openreview.net/forum?id=rJl-b3RcF7`.

Song Han, Jeff Pool, John Tran, and William Dally. Learning both weights and connections for efficient neural network. *Advances in neural information processing systems*, 28, 2015.

Woo Kyoung Han, Byeonghun Lee, Hyunmin Cho, Sunghoon Im, and Kyong Hwan Jin. Towards lossless implicit neural representation via bit plane decomposition. In *Proceedings of the Computer Vision and Pattern Recognition Conference*, pages 2269–2278, 2025.

Babak Hassibi, David G Stork, and Gregory J Wolff. Optimal brain surgeon and general network pruning. In *IEEE international conference on neural networks*, pages 293–299. IEEE, 1993.

Torsten Hoefler, Dan Alistarh, Tal Ben-Nun, Nikoli Dryden, and Alexandra Peste. Sparsity in deep learning: Pruning and growth for efficient inference and training in neural networks. *The Journal of Machine Learning Research*, 22(1):10882–11005, 2021.

Dhananjaya Jayasundara, Sudarshan Rajagopalan, Yasiru Ranasinghe, Trac D Tran, and Vishal M Patel. Sinr: Sparsity driven compressed implicit neural representations. In *Proceedings of the Computer Vision and Pattern Recognition Conference*, pages 3061–3070, 2025.

Adam Kania, Marko Mihajlovic, Sergey Prokudin, Jacek Tabor, PrzemysĹ Spurek, et al. Fresh: Frequency shifting for accelerated neural representation learning. *arXiv preprint arXiv:2410.05050*, 2024.

Bernhard Kerbl, Georgios Kopanas, Thomas Leimkühler, and George Drettakis. 3d gaussian splatting for real-time radiance field rendering. *ACM Transactions on Graphics*, 42(4), July 2023. URL https://repo-sam.inria.fr/fungraph/3d-gaussian-splatting/.

Diederik P. Kingma and Jimmy Ba. Adam: A method for stochastic optimization. In Yoshua Bengio and Yann LeCun, editors, *3rd International Conference on Learning Representations, ICLR 2015, San Diego, CA, USA, May 7-9, 2015, Conference Track Proceedings*, 2015. URL http://arxiv.org/abs/1412.6980.

Yann LeCun, John Denker, and Sara Solla. Optimal brain damage. *Advances in neural information processing systems*, 2, 1989.

Jaeho Lee, Jihoon Tack, Namhoon Lee, and Jinwoo Shin. Meta-learning sparse implicit neural representations. *Advances in Neural Information Processing Systems*, 34:11769–11780, 2021.

David B Lindell, Dave Van Veen, Jeong Joon Park, and Gordon Wetzstein. Bacon: Band-limited coordinate networks for multiscale scene representation. In *Proceedings of the IEEE/CVF conference on computer vision and pattern recognition*, pages 16252–16262, 2022.

Zhen Liu, Hao Zhu, Qi Zhang, Jingde Fu, Weibing Deng, Zhan Ma, Yanwen Guo, and Xun Cao. Finer: Flexible spectral-bias tuning in implicit neural representation by variable-periodic activation functions. In *Proceedings of the IEEE/CVF Conference on Computer Vision and Pattern Recognition*, pages 2713–2722, 2024.

Ishit Mehta, Michaël Gharbi, Connelly Barnes, Eli Shechtman, Ravi Ramamoorthi, and Manmohan Chandraker. Modulated periodic activations for generalizable local functional representations. In *Proceedings of the IEEE/CVF International Conference on Computer Vision*, pages 14214–14223, 2021.

Ishit Mehta, Manmohan Chandraker, and Ravi Ramamoorthi. A level set theory for neural implicit evolution under explicit flows. In *European Conference on Computer Vision*, pages 711–729. Springer, 2022.

Gaurav Menghani. Efficient deep learning: A survey on making deep learning models smaller, faster, and better. *ACM Computing Surveys*, 55(12):1–37, 2023.

Ben Mildenhall, Pratul P Srinivasan, Matthew Tancik, Jonathan T Barron, Ravi Ramamoorthi, and Ren Ng. Nerf: Representing scenes as neural radiance fields for view synthesis. *Communications of the ACM*, 65(1):99–106, 2021.

Tiago Novello. Understanding sinusoidal neural networks. *arXiv preprint arXiv:2212.01833*, 2022.

Tiago Novello, Guilherme Schardong, Luiz Schirmer, Vinicius da Silva, Helio Lopes, and Luiz Velho. Exploring differential geometry in neural implicits. *Computers & Graphics*, 108:49–60, 2022.

Tiago Novello, Vinicius da Silva, Guilherme Schardong, Luiz Schirmer, Helio Lopes, and Luiz Velho. Neural implicit surface evolution. In *Proceedings of the IEEE/CVF International Conference on Computer Vision*, pages 14279–14289, 2023.

Tiago Novello, Diana Aldana, Andre Araujo, and Luiz Velho. Tuning the frequencies: Robust training for sinusoidal neural networks. In *Proceedings of the IEEE/CVF Conference on Computer Vision and Pattern Recognition*, 2025.

Adam Paszke, Sam Gross, Francisco Massa, Adam Lerer, James Bradbury, Gregory Chanan, Trevor Killeen, Zeming Lin, Natalia Gimelshein, Luca Antiga, et al. Pytorch: An imperative style, high-performance deep learning library. *Advances in neural information processing systems*, 32, 2019.

Hallison Paz, Daniel Perazzo, Tiago Novello, Guilherme Schardong, Luiz Schirmer, Vinicius da Silva, Daniel Yukimura, Fabio Chagas, Helio Lopes, and Luiz Velho. Mr-net: Multiresolution sinusoidal neural networks. *Computers & Graphics*, 2023.

Hallison Paz, Tiago Novello, and Luiz Velho. Implicit neural representation of tileable material textures, 2024.

Vishwanath Saragadam, Jasper Tan, Guha Balakrishnan, Richard G Baraniuk, and Ashok Veeraraghavan. Miner: Multiscale implicit neural representation. In *European Conference on Computer Vision*, pages 318–333. Springer, 2022.

Vishwanath Saragadam, Daniel LeJeune, Jasper Tan, Guha Balakrishnan, Ashok Veeraraghavan, and Richard G Baraniuk. Wire: Wavelet implicit neural representations. In *Proceedings of the IEEE/CVF Conference on Computer Vision and Pattern Recognition*, pages 18507–18516, 2023.

Hemanth Saratchandran, Sameera Ramasinghe, and Simon Lucey. From activation to initialization: Scaling insights for optimizing neural fields. In *Proceedings of the IEEE/CVF Conference on Computer Vision and Pattern Recognition*, pages 413–422, 2024.

Hemanth Saratchandran, Sameera Ramasinghe, Violetta Shevchenko, Alexander Long, and Simon Lucey. A sampling theory perspective on activations for implicit neural representations. In *Proceedings of the 41st International Conference on Machine Learning*, ICML'24. JMLR.org, 2025.

Guilherme Schardong, Tiago Novello, Hallison Paz, Iurii Medvedev, Vinícius Da Silva, Luiz Velho, and Nuno Gonçalves. Neural implicit morphing of face images. In *Proceedings of the IEEE/CVF Conference on Computer Vision and Pattern Recognition*, pages 7321–7330, 2024.

Luiz Schirmer, Tiago Novello, Vinícius da Silva, Guilherme Schardong, Daniel Perazzo, Hélio Lopes, Nuno Gonçalves, and Luiz Velho. Geometric implicit neural representations for signed distance functions. *Computers & Graphics*, 125:104085, 2024.

Kathan Shah and Chawin Sitawarin. Spder: Semiperiodic damping-enabled object representation. *arXiv preprint arXiv:2306.15242*, 2023.

Kexuan Shi, Xingyu Zhou, and Shuhang Gu. Improved implicit neural representation with fourier reparameterized training. In *Proceedings of the IEEE/CVF Conference on Computer Vision and Pattern Recognition*, pages 25985–25994, 2024.

Vincent Sitzmann, Julien Martel, Alexander Bergman, David Lindell, and Gordon Wetzstein. Implicit neural representations with periodic activation functions. *Advances in neural information processing systems*, 33:7462–7473, 2020.

Matthew Tancik, Pratul Srinivasan, Ben Mildenhall, Sara Fridovich-Keil, Nithin Raghavan, Utkarsh Singhal, Ravi Ramamoorthi, Jonathan Barron, and Ren Ng. Fourier features let networks learn high frequency functions in low dimensional domains. *Advances in Neural Information Processing Systems*, 33:7537–7547, 2020.

Hugo Tessier, Vincent Gripon, Mathieu Léonardon, Matthieu Arzel, Thomas Hannagan, and David Bertrand. Rethinking weight decay for efficient neural network pruning. *Journal of Imaging*, 8(3): 64, 2022.

Georg Thimm and Emile Fiesler. Evaluating pruning methods. In *Proceedings of the International Symposium on Artificial neural networks*, pages 20–25, 1995.

Joanna Waczyńska, Tomasz Szczepanik, Piotr Borycki, Sławomir Tadeja, Thomas Bohné, and Przemysław Spurek. Mirage: Editable 2d images using gaussian splatting. *arXiv preprint arXiv:2410.01521*, 2024.

Zhijie Wu, Yuhe Jin, and Kwang Moo Yi. Neural fourier filter bank. In *Proceedings of the IEEE/CVF Conference on Computer Vision and Pattern Recognition*, pages 14153–14163, 2023.

Guandao Yang, Serge Belongie, Bharath Hariharan, and Vladlen Koltun. Geometry processing with neural fields. *Advances in Neural Information Processing Systems*, 34:22483–22497, 2021.

Taesun Yeom, Sangyoon Lee, and Jaeho Lee. Fast training of sinusoidal neural fields via scaling initialization. *arXiv preprint arXiv:2410.04779*, 2024.

Wang Yifan, Lukas Rahmann, and Olga Sorkine-hornung. Geometry-consistent neural shape representation with implicit displacement fields. In *International Conference on Learning Representations*, 2021.

Gizem Yüce, Guillermo Ortiz-Jiménez, Beril Besbinar, and Pascal Frossard. A structured dictionary perspective on implicit neural representations. In *Proceedings of the IEEE/CVF Conference on Computer Vision and Pattern Recognition*, pages 19228–19238, 2022.

Andreas Zell, Nuri Benbarka, Timon Hoefer, and Hamd Ul Moqueet Riaz. Seeing implicit neural representations as fourier series. In *2022 IEEE/CVF Winter Conference on Applications of Computer Vision (WACV)*. IEEE Computer Society, 2022.

Xinjie Zhang, Xingtong Ge, Tongda Xu, Dailan He, Yan Wang, Hongwei Qin, Guo Lu, Jing Geng, and Jun Zhang. Gaussianimage: 1000 fps image representation and compression by 2d gaussian splatting. In *European Conference on Computer Vision*, pages 327–345. Springer, 2024.

A PROOFS

A.1 THEOREM 1

In the main paper, we present an identity (Thrm 1) derived by Novello et al. (2025), which linearizes the j-th hidden neuron of the $(i+1)$-th layer, h_j^{i+1}. Similar results have been presented in Yüce et al. (2022) for the case of shallow SIRENs. The identity below extends this analysis to hidden neurons at arbitrary depths.

Theorem 3. *The hidden neuron h_j^{i+1} admits the following amplitude-phase expansion:*

$$h_j^{i+1}(\mathbf{x}) = \sum_{\mathbf{k}\in\mathbb{Z}^{n_i}} \alpha_{\mathbf{k}} \sin\left(\langle \mathbf{k}, \mathbf{y}^i\rangle + b_j^{i+1}\right), \qquad \text{where} \quad |\alpha_{\mathbf{k}}| \leq \prod_l \left(\frac{|W_{jl}^{i+1}|}{2}\right)^{|k_l|} \frac{1}{|k_l|!}. \tag{5}$$

Here, $\alpha_{\boldsymbol{k}} = \prod_{l=1}^{n_i} J_{k_l}(W_{jl}^{i+1})$ is the product of Bessel functions.

Before starting the proof, recall that we defined $h_j^{i+1}(\mathbf{x}) = \sin\left(\sum_{l=1}^{n_i} W_{jl}^{i+1}\sin(y_l^i) + b_j^{i+1}\right)$, with $\mathbf{y}^i = \left[y_l^i\right]_l$ the linear, non-activated contribution of the i-th layer. To simplify notation, we drop the indices i and $i+1$ from $\mathbf{W}^{i+1}, \mathbf{b}^{i+1}, \mathbf{y}^i,$ and n_i.

Proof. The first part of the proof consists of verifying

$$\begin{aligned} \sin\left(\sum_{l=1}^{n} W_{jl}\sin(y_l) + b_j\right) &= \sum_{\mathbf{k}\in\mathbb{Z}^m} \alpha_{\mathbf{k}} \sin\left(\langle \mathbf{k}, \mathbf{y}\rangle + b_j\right) \quad \text{and} \\ \cos\left(\sum_{l=1}^{n} W_{jl}\sin(y_l) + b_j\right) &= \sum_{\mathbf{k}\in\mathbb{Z}^m} \alpha_{\mathbf{k}} \cos\left(\langle \mathbf{k}, \mathbf{y}\rangle + b_j\right). \end{aligned} \tag{6}$$

The proof is by induction in n. For the **base** case $n = 1$, we use the sum of angles identities and the Bessel function of the first kind properties (see (Abramowitz and Stegun, 1964, num. 9.1.42, 9.1.43)) to prove $\sin\left(W_{j1}\sin(y_1) + b_j\right) = \sum_{k\in\mathbb{Z}} J_k(W_{j1})\sin(ky_1 + b_j)$:

$$\begin{aligned}
\sin\left(W_{j1}\sin(y_1) + b_j\right) &= \sin\left(W_{j1}\sin(y_1)\right)\cos(b_j) + \cos\left(W_{j1}\sin(y_1)\right)\sin(b_j) \\
&= \sum_{k\in\mathbb{Z}\text{ odd}} J_k(W_{1j})\sin(ky_1)\cos(b_j) + \sum_{l\in\mathbb{Z}\text{ even}} J_l(W_{1j})\cos(ly_1)\sin(b_j) \\
&= \sum_{k\in\mathbb{Z}\text{ odd}} J_k(W_{j1})\sin(ky_1 + b_j) + \sum_{l\in\mathbb{Z}\text{ even}} J_l(W_{j1})\sin(ly_1 + b_j) \\
&= \sum_{k\in\mathbb{Z}} J_k(W_{j1})\sin(ky_1 + b_j).
\end{aligned}$$

In the third equality we combined the formula $\sin(u)\cos(v) = \frac{\sin(u+v)+\sin(u-v)}{2}$ and the fact that $J_{-k}(u) = (-1)^k J_k(u)$ to rewrite the summations. The proof of the cosine analogous expansion $\cos\left(W_{j1}\sin(y_1) + b_j\right) = \sum J_l(W_{j1} + b_j)\cos(ly_1)$ is similar.

Assume that equation 6 hold for $n-1$, with $n > 1$, we prove that it also holds for n (the **induction step**).

$$\begin{aligned}
\sin\left(\sum_{l=1}^{n} W_{jl}\sin(y_l) + b_j\right) &= \sin\left(\sum_{l=1}^{n-1} W_{jl}\sin(y_l) + b_j\right)\cos\left(W_{jn}\sin(y_n)\right) \\
&\quad + \cos\left(\sum_{l=1}^{n-1} W_{jl}\sin(y_l) + b_j\right)\sin\left(W_{jn}\sin(y_n)\right) \\
&= \sum_{\mathbf{k}\in\mathbb{Z}^{n-1},\, l\in\mathbb{Z}\text{ even}} \alpha_{\mathbf{k}} J_l(W_{jn})\sin\Big(\langle\mathbf{k},\mathbf{y}\rangle + b_j\Big)\cos(ly_n) \\
&\quad + \sum_{\mathbf{k}\in\mathbb{Z}^{n-1},\, l\in\mathbb{Z}\text{ odd}} \alpha_{\mathbf{k}} J_l(W_{jn})\cos\Big(\langle\mathbf{k},\mathbf{y}\rangle + b_j\Big)\sin(ly_n) \\
&= \sum_{\mathbf{k}\in\mathbb{Z}^n} \alpha_{\mathbf{k}}\sin\Big(\langle\mathbf{k},\mathbf{y}\rangle + b_j\Big)
\end{aligned}$$

We use the induction hypothesis in the second equality and an argument similar to the one used in the base case to rewrite the harmonic sum. Again, the cosine activation function case is analogous.

For the second part of the proof, we must prove the inequality in Equation equation 1. For that, note that $\alpha_{\mathbf{k}} = \prod_{l=1}^{n} J_{k_l}(W_{jl})$, and that

$$|J_k(W_{jl})| < \frac{\left(\frac{|W_{jl}|}{2}\right)^k}{k!}, \quad k > 0, \quad W_{jl} > 0 \tag{7}$$

But this also holds for $W_{jl} \leq 0$ since $|J_k(-u)| = |J_k(u)|$, and for $k \leq 0$ as $|J_{-k}(u)| = |(-1)^k J_k(u)| = |J_k(u)|$. Then, substituting equation 7 in $\alpha_{\mathbf{k}} = \prod_{l=1}^{n} J_{k_l}(W_{jl})$, we obtain the desired result. □

A.2 THEOREM 2

Theorem 4. *Let f_θ be a sinusoidal INR of depth d, and let $\widetilde{f}_\theta$ be the network obtained by perturbing the k-th hidden layer weights and biases to $\widetilde{\mathbf{W}}^k$ and $\widetilde{\mathbf{b}}^k$. Then,*

$$\sup_{\mathbf{x}} \left\| f_\theta(\mathbf{x}) - \widetilde{f}_\theta(\mathbf{x}) \right\|_\infty \leq \left(\|\mathbf{W}^k - \widetilde{\mathbf{W}}^k\|_\infty + \|\mathbf{b}^k - \widetilde{\mathbf{b}}^k\|_\infty \right) \|\mathbf{L}\|_\infty \prod_{i=k+1}^{d} \|\mathbf{W}^i\|_\infty.$$

Proof. First, note that $\mathbf{x} \mapsto \mathbf{L}\mathbf{x}$ is $\|\mathbf{L}\|_\infty$-Lipschitz for infinity norms:

$$\|\mathbf{L}\mathbf{x} - \mathbf{L}\mathbf{x}'\|_\infty = \|\mathbf{L}(\mathbf{x} - \mathbf{x}')\|_\infty \leq \|\mathbf{L}\|_\infty \|\mathbf{x} - \mathbf{x}'\|_\infty.$$

Second, note that $\mathbf{x} \mapsto \sin(\mathbf{x})$ is 1-Lipschitz also for infinity norms, and thus $\mathbf{x} \mapsto \mathbf{S}^i(\mathbf{x}) = \sin(\mathbf{W}^i\mathbf{x} + \mathbf{b}^i)$ is also $\|\mathbf{W}^i\|_\infty$-Lipschitz:

$$\begin{aligned}\|\sin(\mathbf{W}^i\mathbf{x} + \mathbf{b}^i) - \sin(\mathbf{W}^i\mathbf{x}' + \mathbf{b}^i)\|_\infty &\leq \|\sin\|_{\text{Lip}}\|(\mathbf{W}^i\mathbf{x}' + \mathbf{b}^i) - (\mathbf{W}^i\mathbf{x}' + \mathbf{b}^i)\|_\infty \\ &\leq \|\mathbf{W}^i(\mathbf{x} - \mathbf{x}')\|_\infty \leq \|\mathbf{W}^i\|_\infty\|\mathbf{x} - \mathbf{x}'\|_\infty.\end{aligned}$$

It thus follows that, for any $\mathbf{x}$:

$$\begin{aligned}&\left\|(\mathbf{L} \circ \mathbf{S}^d \circ \cdots \circ \mathbf{S}^k \circ \cdots \circ \mathbf{S}^0)(\mathbf{x}) - (\mathbf{L} \circ \mathbf{S}^d \circ \cdots \circ \widetilde{\mathbf{S}}^k \circ \cdots \circ \mathbf{S}^0)(\mathbf{x})\right\|_\infty \\ &\leq \|\mathbf{L}\|_\infty \left\|(\mathbf{S}^d \circ \cdots \circ \mathbf{S}^k \circ \cdots \circ \mathbf{S}^0)(x) - (\mathbf{S}^d \circ \cdots \circ \widetilde{\mathbf{S}}^k \circ \cdots \circ \mathbf{S}^0)(\mathbf{x})\right\|_\infty \\ &\leq \|\mathbf{L}\|_\infty \left(\prod_{i=k+1}^{d} \|\mathbf{W}^i\|_\infty\right) \left\|(\mathbf{S}^k \circ \cdots \circ \mathbf{S}^0)(\mathbf{x}) - (\widetilde{\mathbf{S}}^k \circ \cdots \circ \mathbf{S}^0)(\mathbf{x})\right\|_\infty \\ &= \|\mathbf{L}\|_\infty \left(\prod_{i=k+1}^{d} \|\mathbf{W}^i\|_\infty\right) \Big\|\sin(\mathbf{W}^k(\mathbf{S}^{k-1} \circ \cdots \circ \mathbf{S}^0)(\mathbf{x}) + \mathbf{b}^k) \\ &\qquad\qquad - \sin(\widetilde{\mathbf{W}}^k(\mathbf{S}^{k-1} \circ \cdots \circ \mathbf{S}^0)(\mathbf{x}) + \widetilde{\mathbf{b}}^k)\Big\|_\infty \\ &\leq \|\mathbf{L}\|_\infty \left(\prod_{i=k+1}^{d} \|\mathbf{W}^i\|_\infty\right) \|\sin\|_{\text{Lip}} \Big\|(\mathbf{W}^k(\mathbf{S}^{k-1} \circ \cdots \circ \mathbf{S}^0)(\mathbf{x}) + \mathbf{b}^k) \\ &\qquad\qquad - (\widetilde{\mathbf{W}}^k(\mathbf{S}^{k-1} \circ \cdots \circ \mathbf{S}^0)(\mathbf{x}) + \widetilde{\mathbf{b}}^k)\Big\|_\infty \\ &= \|\mathbf{L}\|_\infty \left(\prod_{i=k+1}^{d} \|\mathbf{W}^i\|_\infty\right) \left\|(\mathbf{W}^k - \widetilde{\mathbf{W}}^k)(\mathbf{S}^{k-1} \circ \cdots \circ \mathbf{S}^0)(\mathbf{x}) + (\mathbf{b}^k - \widetilde{\mathbf{b}}^k)\right\|_\infty \\ &\leq \|\mathbf{L}\|_\infty \left(\prod_{i=k+1}^{d} \|\mathbf{W}^i\|_\infty\right) \left(\left\|(\mathbf{W}^k - \widetilde{\mathbf{W}}^k)(\mathbf{S}^{k-1} \circ \cdots \circ \mathbf{S}^0)(\mathbf{x})\right\|_\infty + \left\|\mathbf{b}^k - \widetilde{\mathbf{b}}^k\right\|_\infty\right) \\ &\leq \|\mathbf{L}\|_\infty \left(\prod_{i=k+1}^{d} \|\mathbf{W}^i\|_\infty\right) \left(\|\mathbf{W}^k - \widetilde{\mathbf{W}}^k\|_\infty \left\|(\mathbf{S}^{k-1} \circ \cdots \circ \mathbf{S}^0)(\mathbf{x})\right\|_\infty + \left\|\mathbf{b}^k - \widetilde{\mathbf{b}}^k\right\|_\infty\right).\end{aligned}$$

Finally, note that since sines lie in $[-1, +1]$, it must hold that $\left\|(\mathbf{S}^{k-1} \circ \cdots \circ \mathbf{S}^0)(\mathbf{x})\right\|_\infty = \max_i \left|[(\mathbf{S}^{k-1} \circ \cdots \circ \mathbf{S}^0)(\mathbf{x})]_i\right| \leq \max_i 1 = 1$, from which we conclude the proof. □

B SIGNED DISTANCE FUNCTIONS

Table 5: Quantitative comparisons on representing surfaces from the Stanford 3D Scanning Repository with $\omega_0 = 30$. We compare the adapted network trained with \method{}, the large network with standard training (large), and the model with small architecture and standard training (small). We report the average chamfer distance (Avg CD ($\times 10^2$)) between reconstructed and ground-truth surfaces and the percentage of network parameters compared to the large architecture (lower is better).

Model (SDFs)	**Variant**	**CD (×10²) ↓**	**Size reduct. ↑**
SIREN	Large	**0.56 ± 0.08**	-
	Small	0.59 ± 0.09	62.14
	Ours	0.58 ± 0.06	62.14
FINER	Large	**0.63 ± 0.09**	-
	Small	0.67 ± 0.09	62.14
	Ours	**0.63 ± 0.06**	62.14

In Table 5 we evaluate AIRe ('Ours') against an overparametrized, large INR of size [256, 256, 256] and a small, reduced model of size [128, 128, 256]. These last two are fitted with the standard training pipeline, and the reconstruction quality was measured using the Chamfer Distance ($\times 10^2$).

Table 6 shows a per-scene breakdown of the SDF quantitative results presented in the main paper when $\omega_0 = 60$ and and the small network size is $[64, 64, 256]$. The per-scene breakdown is consistent with the aggregate quantitative metrics. Our method outperforms the small network in all cases. It also obtains similar or better accuracy compared to the large network but uses roughly 1/6 of network parameters.

Table 6: Per-scene quantitative comparisons on representing surfaces from the Stanford 3D Scanning Repository with $\omega_0 = 60$ and model size $[64, 64, 256]$. We compare AIRe, the network with large architecture, and the model with small architecture. We report the chamfer distance (CD ($\times 10^2$)) between reconstructed and ground-truth surfaces (lower is better). Best values in **bold**, second best values underlined.

Model	Variant	CD ($\times 10^2$) ↓				
		Armadillo	Bunny	Dragon	Happy Buddha	Lucy
SIREN	Large	**0.60**	0.75	0.65	**0.50**	0.74
	Small	0.99	0.79	0.82	0.98	0.86
	Ours	0.65	**0.69**	**0.62**	0.64	**0.61**
FINER	Large	2.13	2.06	2.17	2.74	1.60
	Small	5.51	10.80	4.57	2.58	1.92
	Ours	**0.88**	**0.95**	**0.73**	**1.10**	**0.76**

Figure 7 shows additional examples of surface reconstructions using SIREN with $\omega_0 = 60$ and model architecture $[64, 64, 256]$. As in the other examples, the surface trained using our method presented a lower error compared to the small network. We also see in Figure 8 an example using FINER with settings $\omega_0 = 60$ and network architecture $[64, 64, 256]$. Note that AIRe offers a better reconstruction than the small network with less artifacts.

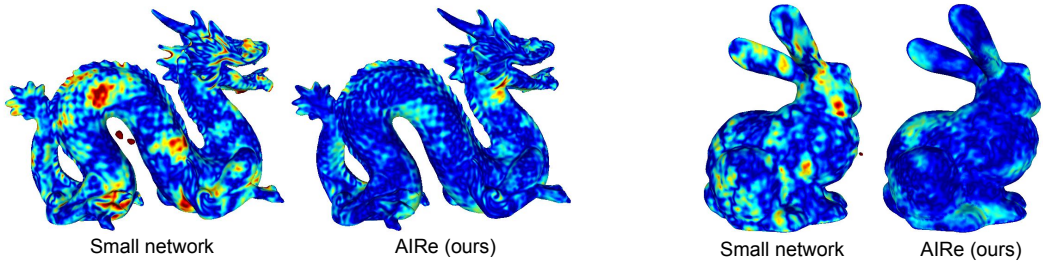

Figure 7: Additional qualitative comparisons on representing surfaces based on the Dragon and Bunny models using a SIREN network with $\omega_0 = 60$ and model architecture $[64, 64, 256]$. Left: results of training the small network. Right: results of AIRe. We illustrate the unsigned distance from the ground-truth surface using a color scale from dark blue (zero) to dark red (≥ 0.01).

We also present Table 7, where we compare the time overhead when training the large, small and adapted models,. Observe that the AIRe and the large model have an equivalent training time but with only 16.04% of the original parameters. Furthermore, observe that a small model trained during the same amount of time has much worse accuracy than a network trained with AIRe.

Neural SDF evolution. Finally, we evaluated AIRe on a surface-smoothing task governed by the mean curvature equation, a classical PDE widely used in geometry processing (Mehta et al., 2022; Yang et al., 2021). In this setting, the network parametrizes a 4D solution $f : \mathbb{R}^4 \to \mathbb{R}$ of

$$\frac{\partial f}{\partial t} = \alpha \operatorname{div}\left(\frac{\nabla_{\mathbf{x}} f}{\|\nabla_{\mathbf{x}} f\|}\right), \quad \text{subject to} \quad f(\mathbf{x}, 0) = g(\mathbf{x}),$$

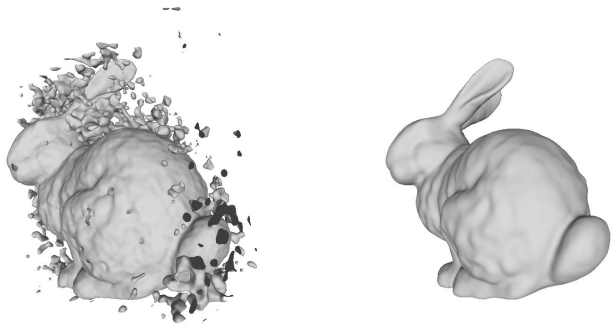

Figure 8: A case with the Bunny model using a FINER network with $\omega_0 = 60$ and model size $[64, 64, 256]$. The final, small network (left) presents several artifacts, which does not occur with the AIRe method (right).

Table 7: **Time overhead comparisons when training SDFs.** We consider a *Large* network with $\sim 133K$ parameters and a *Small* network with $\sim 22K$ parameters that are fitted for 1000 epochs. We compare them with a network adapted during 1000 epochs using AIRe up to a size equal to the small network. We also train the final network for 2000 epochs to compare the reconstruction quality along a time budget.

Variant	CD ($\times 10^2$) ↓	Size reduct. ↑	Time (s) ↓
Large	0.65	-	76.0
Small (10^3 ep)	0.89	83.96%	39.4
Small (2×10^3 ep)	0.86	83.96%	83.2
Ours	0.64	83.96%	76.8

SDF	Large	Small (10^3 ep)	Small (2×10^3 ep)	Ours
Armadillo	52	27	55	52
Bunny	34	17	35	34
Dragon	60	31	65	60
Happy Buddha	159	83	179	162
Lucy	75	39	82	76
Avg. time (s)↓	76.0	39.4	83.2	76.8

where g is the SDF of the initial surface, $\nabla_{\mathbf{x}} f$ is the spatial gradient, div denotes the divergence operator, and α controls the smoothing rate. We adapted AIRe within the NISE framework (Novello et al., 2023) to solve this PDE using the Armadillo SDF as the initial condition, over the time interval $t \in [0, 0.2]$, with $\alpha = 0.001$. The network f was trained during 10000 epochs using an oriented point cloud of size ≈ 173000. During training, we used minibatches of 15000 on-surface points, 15000 off-surface points, and 30000 in $\mathbb{R}^3 \times [-1, 1]$.

We begin with an architecture of [256, 256, 256] and prune approximately 34% of its parameters by removing 25% of the neurons from the first two layers. We then compare the resulting evolution against a baseline obtained by training the original (larger) network from scratch. Since no ground-truth evolution is available for this task, we evaluate the result by reconstructing the evolved surfaces at $t = 0.0,\ 0.1,\ 0.2$ for both models and computing the CD between them, obtaining an average error of 0.004. This indicates that AIRe adapts the network while preserving the accuracy of the geometric evolution. Figure 9 shows the reconstructed surfaces at these three time steps; as expected, regions of high curvature contract as the surface smooths over time.

C IMAGES

In Figure 10, we evaluate the effect of our densification and pruning schemes on both training convergence and spectral stability. Our training procedure begins with an initial fitting stage, followed by a densification step in which newly added input neurons are initialized with small contributions (via low column norms) to prevent a spike in the loss. The model is then fine-tuned (blue region in the training curve), which produces a sharp drop in training error and increases the contributions of the added neurons (see Figure 10, bottom). As a result, most newly added neurons are no longer classified as low-contribution (orange points) by the time TWD begins.

After selecting candidate neurons for pruning, we apply TWD to progressively reduce their influence on the output. This regularization introduces a small bump in the loss near epoch 2400, but the curve

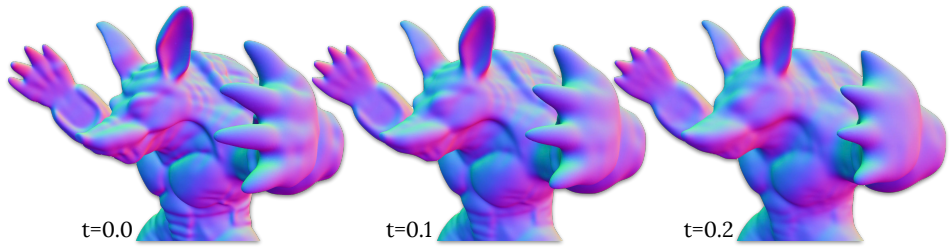

Figure 9: **Surface smoothing via mean curvature flow using AIRe.** Reconstructed time steps ($t = 0.0$, $t = 0.1$, $t = 0.2$) of the Armadillo model evolving under the mean curvature equation. Despite pruning approximately 34% of the parameters, AIRe accurately captures the geometric evolution, achieving a final CD of 0.004 with respect to the baseline large model.

quickly stabilizes and remains below the loss achieved by the large network. Furthermore, TWD mitigates the discontinuity normally caused by pruning, as it minimizes the discrepancy between the reconstructions immediately before and after the pruning step. This effect is illustrated in Figure 10 (top-right), which shows the difference between the Fourier transforms of the reconstructed signal before and after pruning: pruning without TWD produces significant spectral artifacts, whereas pruning with TWD preserves the spectrum much more faithfully.

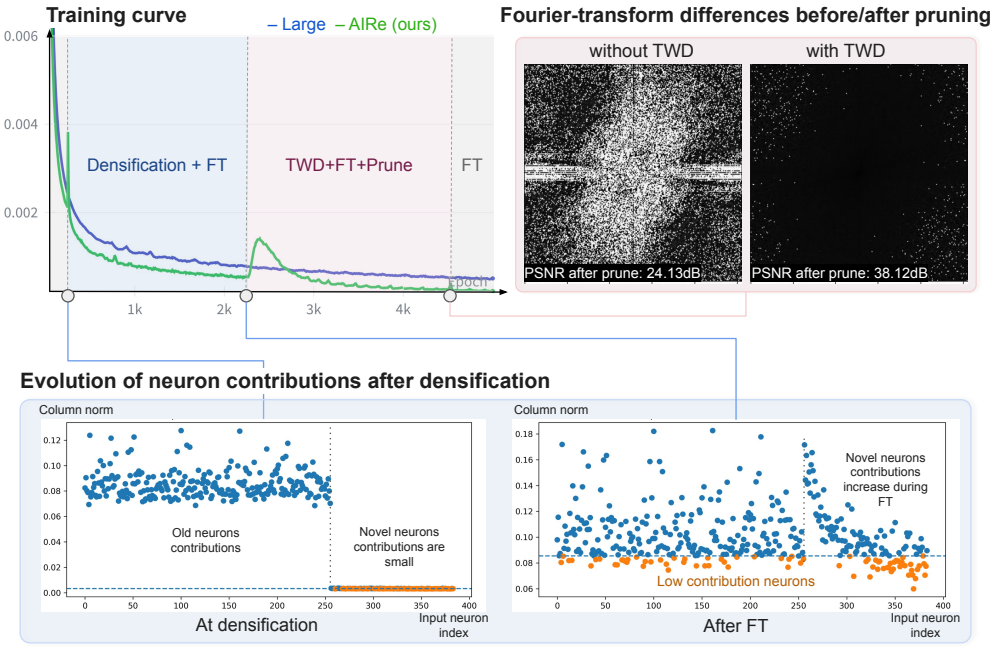

Figure 10: **Effect of densification and pruning on convergence and spectral stability.** *Top left:* Training curve showing the stages of AIRe (initial fitting; densification; fine-tuning; TWD followed by pruning). *Top right:* Fourier-transform differences between reconstructed signals before and after pruning, comparing pruning without TWD and with TWD. Pruning without TWD leads to strong spectral distortion (PSNR 24.13dB), whereas pruning with TWD preserves the spectrum (PSNR 38.12dB). *Bottom:* Evolution of neuron contributions after densification. Left: at densification time, newly added neurons have small norms. Right: after fine-tuning, the contributions of novel neurons increase, while low-contribution neurons (orange) become clear pruning candidates.

Table 8: **AIRe applied to SPDER architecture.**

Model (Images)	Variant	PSNR↑	Size reduct.↑
SPDER	Large	30.77	–
SPDER	Ours	34.61	34.89%

Performance evaluation. Table 8 evaluates AIRe on the SPDER architecture in the DIV2K dataset, using the same model size and training configuration as in Table 1. We use 90% of the pixels for training and 10% for computing PSNR. As shown in the table, AIRe improves reconstruction quality by nearly 4dB while reducing the number of parameters by 34.89%, demonstrating its ability to effectively adapt distinct INR architectures to a given signal.

Table 9: **Inference performance for the image task.**

Variant	CPU inf. time (s)↓	GPU inf. time ($\times 10^{-4}$ s)↓	GPU avg usage (%)↓
Large	0.74	4.32	44.17
Ours	0.61	3.19	31.53
Improvement	17.16%	26.17%	28.62%

Table 9 reports the CPU/GPU inference time and the average GPU usage for the image models trained in Table 3. Each measurement was repeated four times per network to ensure robustness. Our method achieves a reduction of 17.16% in CPU inference time and 26.17% in GPU inference time, while also lowering average GPU utilization by 28.62%. This reduction in resource usage enables larger image batches to be processed during inference.

Additional ablations. We present ablation studies to support the choice of hyperparameters for AIRe. First, we investigate the optimal allocation of epochs between the targeted weight decay stage and the fine-tuning stage under a fixed training budget. Specifically, we train SIREN Sitzmann et al. (2020) and FINER Liu et al. (2024) models, each with two hidden layers of 512 neurons, for a total of 5000 epochs. Training begins with standard optimization for x epochs, followed by targeted weight decay for y epochs, where $x, y \in \{100, 750, 1000, 1250, 1500, 1750, 2000, 2250\}$. The remaining $5000 - x - y$ epochs are allocated to fine-tuning.

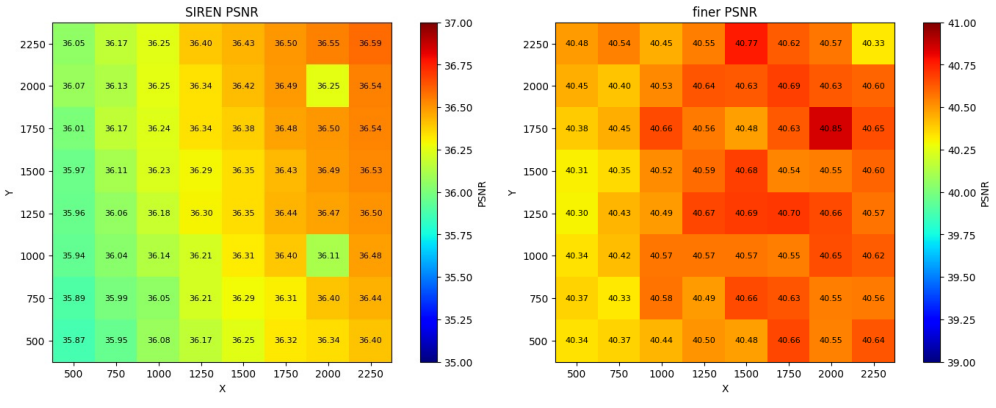

Figure 11: Ablation of the number of epochs used to pre-train the model (x axis), to train with targeted weight decay (y axis) and fine tune. The total training lasts for 5000 epochs, and each value refers to the mean PSNR over the DIV2K dataset. (Left) SIREN Sitzmann et al. (2020) architecture shows that longer standard training and targeted weight decay stage improve quality, even with fewer fine tuning epochs. (Right) FINER architecture shows less consistency in the results, demonstrating that above 1000 epochs of standard training the results improve, but show no clear pattern.

Figure 11 shows the PSNR for each epoch distribution, where the x-axis corresponds to the number of epochs used for the initial standard training stage, and the y-axis indicates the number of epochs

allocated to the targeted weight decay stage. As shown, SIREN models benefit from increased training time in both the standard training and targeted weight decay stages, resulting in improved reconstruction accuracy. In contrast, FINER models show only marginal improvements when the initial training stage exceeds 1000 epochs.

To determine the optimal pruning configuration, both in terms of which layers to prune and the amount per layer, we train models with the best-performing epoch distribution for both SIREN and FINER over 5000 epochs, applying varying levels of pruning to each layer. Figure 12 presents the PSNR of each reconstruction, where x represents the percentage of neurons pruned in the first layer, and y denotes the percentage pruned in the second layer.

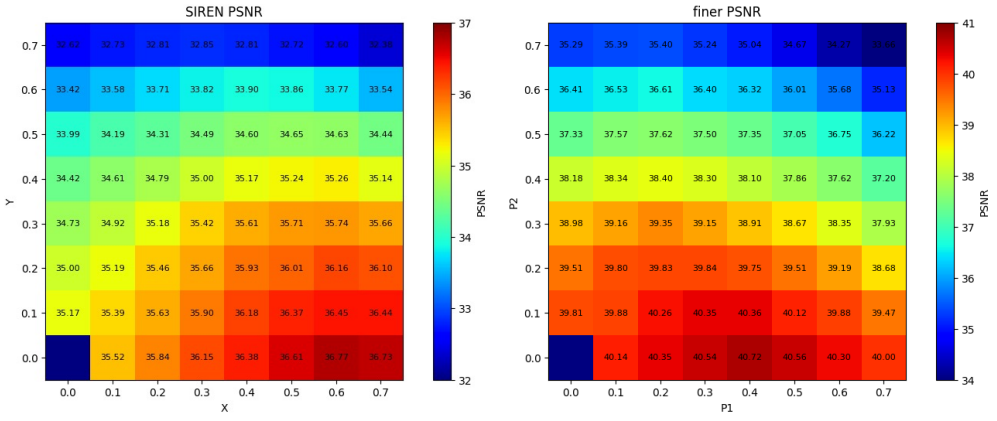

Figure 12: Ablation of the quality degradation with respect to the percentage of prune on the input neurons (x axis) and the 1st hidden neurons (y axis). The total training lasts for 5000 epochs, and each value refers to the mean PSNR over the DIV2K dataset. Observe that both images show that pruning the 1st layer retains more quality than pruning the 2nd layer. (Left) A SIREN Sitzmann et al. (2020) architecture reconstruction quality is preserved even with an extreme prune of 60%. (Right) FINER architecture quality is better retained when pruning the first layer, albeit with less percentage.

Both SIREN and FINER benefit from pruning the input neurons, although the optimal percentage of neuron removal differs between the two. In contrast, pruning hidden neurons generally leads to a degradation in reconstruction quality.

We also perform an ablation study on the use of regularization to improve neuron removal during training. Specifically, we train a sinusoidal INR using three configurations: standard weight decay, targeted weight decay, and no regularization prior to pruning. Standard weight decay yields the lowest reconstruction accuracy at 34.2dB, while removing regularization improves the result by 0.51dB. The targeted weight decay stage achieves the best performance, increasing accuracy to 36.9 dB.

For the densification strategy, we examine the impact of varying both the number of training epochs before densification and the percentage of new input neurons added. Concretely, the INR is initially trained for x epochs, then its first layer is expanded by $(y * 100)\%$, and the augmented network is fine-tuned for the remaining $3000 - x$ epochs. The results are presented in Figure 13.

As expected, increasing the number of neurons leads to higher PSNR values. Additionally, accuracy improves when a larger number of neurons is added early in the training process (i.e., before 1500 epochs).

D Additional Discussions

We provide further details regarding the parameter settings used in our experiments. The targeted weight decay stage is trained using the following loss function

$$\mathcal{L}_{\alpha,\mathcal{I}} = \mathcal{L}_{\text{data}} + \alpha \sum_{j \in \mathcal{I}} \|\mathbf{W}_{*j}\|_1,$$

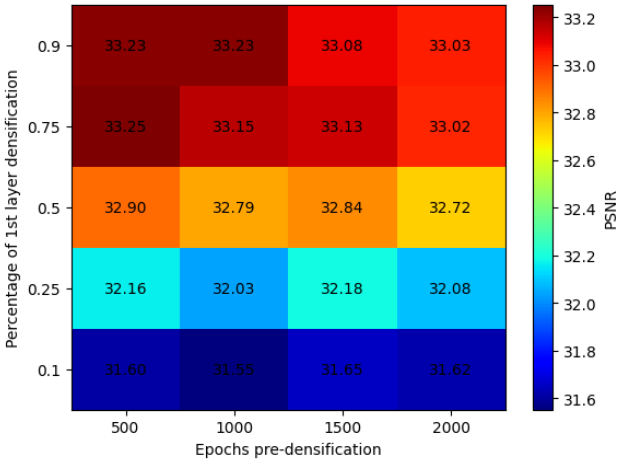

Figure 13: Ablation on the epochs trained before densifying (x axis) compared to the percentage of input neurons added (y axis).

where α is a parameter that starts at zero and increases linearly up to one at the end of this stage. For the pruning scheme, we use the Prune package in PyTorch, using structured masks over the to remove the corresponding weights. Specifically, when pruning neuron h_j^i, we mask the entries of the j-th column of $\mathbf{W}^i$. This removes all the neuron's influence from the network. As for the densification technique, we preserve the optimizer state of previous neurons to minimize training affectation.

We trained using a 12 GB NVIDIA GPU (TITAN X Pascal) and a 24 GB NVIDIA GPU (RTX 4090).

D.1 Neural Radiance Fields

We evaluate the forward-pass latency, computational cost (GFLOPs) for the large SIREN model and our pruned architecture (AIRe) on the trained models in Table 1. The results are summarized in Table 10.

These results show that computational cost is reduced by $\approx 31\%$, consistent with the structural sparsity introduced by our pruning mechanism. This indicates that removing neurons and reducing FLOPs directly accelerates the forward pass on GPU. Overall, these measurements confirm that our architectural adaptation yields meaningful improvements in GPU inference latency, which is the critical metric for real-time or high-resolution INR workloads.

Table 10: **Inference efficiency comparison.**

Variant	**Gflops**
Large	7.49
AIRe	5.17
Improv.	30.96%

We adopt the torch-ngp framework [2] for NeRF implemented by FINER that considers two networks: A density network that takes a 3D position as input and outputs a density value and a geometric feature vector $v \in \mathbb{R}^{182}$; and a color network that receives v and a 3D direction and returns a RGB color. NeRF computes the color of a pixel with volume rendering using 3D points sampled on a ray traced from the center of the virtual camera through the pixel Mildenhall et al. (2021). We set the batch size to $4,096$ rays and Adam optimizer with learning rate of 0.0002, $\beta_1 = 0.9$, $\beta_1 = 0.99$, $\epsilon = 10^{-15}$, and exponential learning rate decay of 0.1. We update the model weights using an exponential moving average with a decay of 0.95. We follow FINER's experimental setting, where for each scene of the Blender dataset, we have 25 images for training, 200 images for testing, all downsampled to 200×200 pixels. We employ the PSNR and the number of network parameters (Params) as evaluation metrics.

We evaluate three approaches for NeRF training: **Large** and **Small** networks, which train from scratch for 1.5×10^3 epochs a density network of size $[182, 182, 182]$ and color networks with architecture $[182, 182, 182]$ and $[91, 91, 182]$, respectively. On the other hand, **AIRe** considers training from scratch for 300 epochs the same networks from Large model, then selecting 50% of the input neurons

[2] https://github.com/ashawkey/torch-ngp

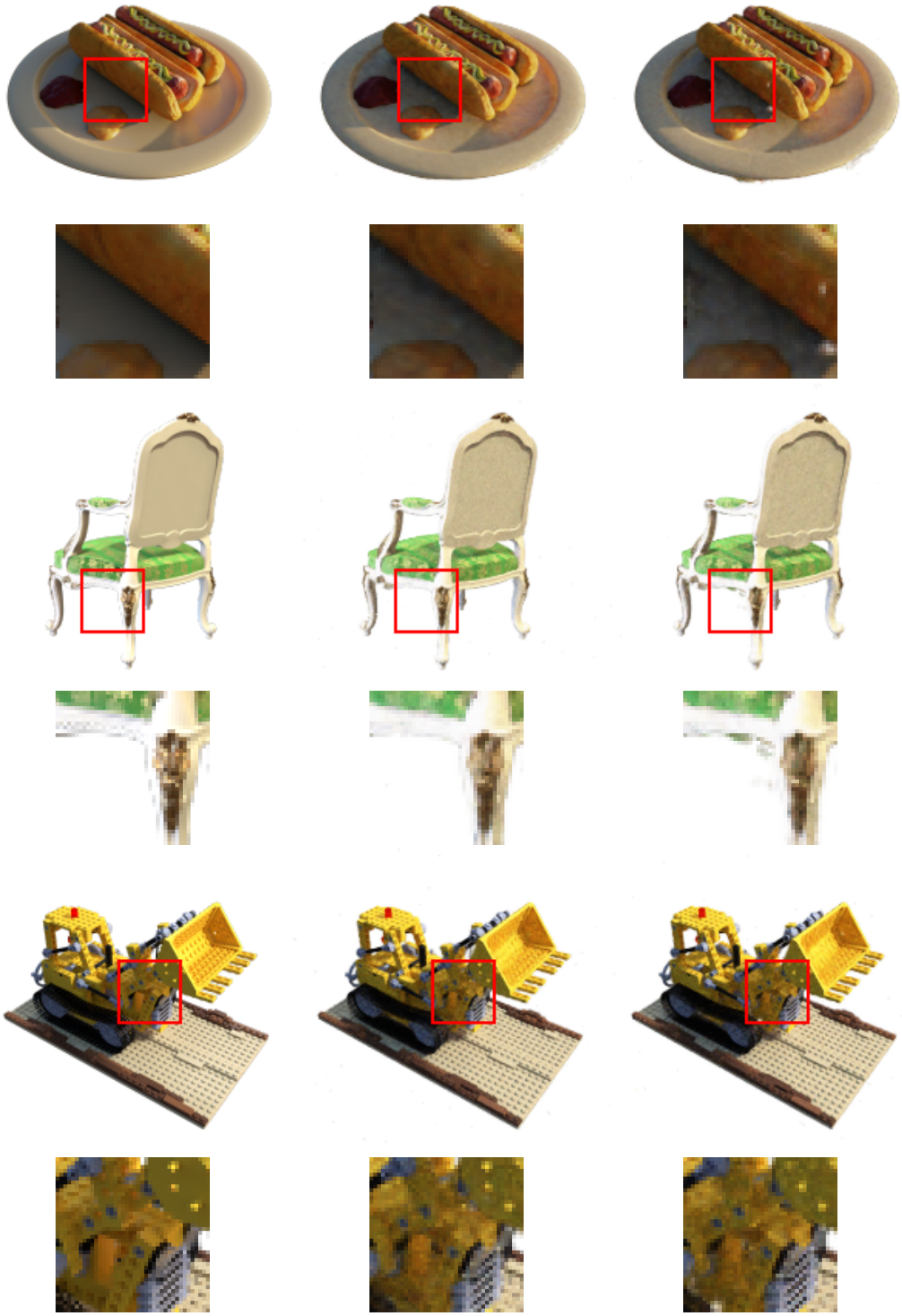

Figure 14: Qualitative comparisons on representing NeRFs using the Hotdog (top), Chair (middle), and Lego (bottom) scenes from the Blender dataset. First column: ground-truth views. Second column: results of our proposed approach of targeted weight decay for pruning (TWD+P). Third column: results of training from scratch a small network (Small) with an architecture equivalent to ours after pruning. Differences in quality highlighted by insets.

and the first hidden neurons of the density network for 750 epochs of TWD, followed by pruning of selected neurons, and finally 450 epochs of fine-tuning of both density and color networks.

Table 11: Quantitative comparisons between AIRe's pruning scheme with training from scratch the 'Large' and 'Small' networks. We report the average PSNR between reconstructed and ground-truth test views (higher is better), the PSNR difference with respect to Large (higher is better), and the percentage of network parameters with respect to Large (higher is better). Best values in **bold**, second best values underlined.

	Method	Chair	Drums	Ficus	Hotdog	Lego	Materials	Mic	Ship	Avg	Size reduct.
PSNR↑	Large	**34.04**	**24.81**	**28.84**	**33.42**	**29.96**	**27.01**	**33.96**	**22.55**	**29.32**	-
	Small	33.12	24.14	27.77	32.06	28.75	26.47	33.68	22.28	28.53	**20.74%**
	Ours	33.23	24.11	27.82	33.10	28.82	26.21	33.59	22.26	28.64	**20.74%**

Table 11 shows that compared to Large, the decrease in PSNR of AIRe was 13.9% lower than the PSNR of the Small network approach, even when both have the same number of network parameters. The pruning procedure allows our NeRF to save more than 20% of network parameters compared to the Large approach. We also see qualitative improvements compared to the Small network, such as shadows/bright spots in the Hotdog (see Figure 1).